

Thermal stability of winds driven by radiation pressure in super-Eddington accretion disks

C. Pinto,^{1,2*} M. Mehdipour,³ D. J. Walton,² M. J. Middleton,⁴ T. P. Roberts,⁵
A. C. Fabian,² M. Guainazzi,¹ R. Soria,^{6,7,8} P. Kosec,² and J.-U. Ness⁹

¹ESTEC/ESA, Keplerlaan 1, 2201AZ Noordwijk, The Netherlands

²Institute of Astronomy, Madingley Road, CB3 0HA Cambridge, United Kingdom

³SRON Netherlands Institute for Space Research, Sorbonnelaan 2, 3584 CA Utrecht, The Netherlands

⁴Physics & Astronomy, University of Southampton, Southampton, Hampshire SO17 1BJ, UK

⁵Centre for Extragalactic Astronomy, Durham University, Department of Physics, South Road, Durham DH1 3LE, UK

⁶College of Astronomy and Space Sciences, University of the Chinese Academy of Sciences, Beijing 100049, China

⁷International Centre for Radio Astronomy Research, Curtin University, GPO Box U1987, Perth, WA 6845, Australia

⁸Sydney Institute for Astronomy, School of Physics A28, The University of Sydney, Sydney, NSW 2006, Australia

⁹ESAC/ESA European Space Astronomy Center, P.O. Box 78, 28691 Villanueva de la Canada, Madrid, Spain

18 March 2019

ABSTRACT

It is currently thought that the vast majority of ultraluminous X-ray sources (ULXs) is powered by neutron stars and stellar-mass black holes accreting at rates which may exceed the Eddington limit by factors of a few up to hundreds. At these high accretion rates, radiation pressure is expected to inflate the accretion disk and drive fast winds at significant fractions of the speed of light. Evidence of such winds has been found in recent work with high-resolution grating spectrometers (RGS) aboard XMM-Newton as well as moderate-resolution detectors. The thick disk structure and the spectral energy distribution resembling those of a broadened disk significantly differ from those of thin disk accretors such as sub-Eddington active galactic nuclei and X-ray binaries. The thermal status of ULX winds, and of super-Eddington accretors in general, is therefore expected to depart from sub-Eddington accreting objects. Here we show the first attempt to calculate the photoionization balance of the winds driven by strong radiation pressure in thick disks with a focus on ULXs, and the effects of different viewing angles. We find that the winds are generally in thermally stable equilibrium, but long-term variations in the accretion rate and the inclination due to precession may have significant effects on the appearance and stability. These trends can explain the correlation between the spectral residuals around 1 keV and ULX spectral state. We also find a possible correlation between the spectral hardness of the ULX, the wind velocity and the ionization parameter in support of the general scenario.

Key words: plasmas – atomic processes – techniques: spectroscopic – X-rays: general – Accretion disks – ultraluminous X-ray sources

1 INTRODUCTION

It is thought that when the Universe was young, black holes were accreting matter at impressive rates in order to build up “fully grown” supermassive black holes with masses of $\gtrsim 10^9 M_\odot$ in a few hundred million years (see, e.g., Fan et al. 2003, Volonteri et al. 2003). At accretion rates approaching the Eddington limit, \dot{M}_E , radiation pressure inflates the thin disk producing a geometry similar to that of a funnel (see, e.g., Shakura & Sunyaev 1973) and a wind is launched (see,

e.g., Poutanen et al. 2007). These systems significantly differ from most common active galactic nuclei (AGN) and X-ray binaries (XRBs) which accrete at sub-Eddington rates (see, e.g., Grimm et al. 2002; Aird et al. 2018). Winds driven by radiation pressure in a super-Eddington (or supercritical) regime can reach mildly-relativistic $\sim 0.1c$ velocities (see, e.g., Takeuchi et al. 2013) and therefore may carry out a huge amount of matter and kinetic power, potentially altering both the accretion onto the black hole and the star-formation in the host galaxy (Feedback, see, e.g., Fabian 2012 and references therein).

* E-mail: ciro.pinto@esa.int

1.1 Highly-accreting supermassive black holes

Nowadays, it is still difficult to study the most distant ($z > 6$) and rare quasars, but there is evidence that some nearby supermassive black holes are accreting at significant fractions of the Eddington limit or beyond such as those powering Narrow Line Seyfert 1 galaxies (NLS1, e.g. Boroson 2002). However, it is difficult to determine the Bolometric luminosity in Eddington units of NLS1s as most disk emission is produced in the UV, significantly affected by interstellar absorption and several systematic effects by up to an order of magnitude, similarly to the highly uncertain mass estimates (see, e.g., Vasudevan & Fabian 2007; Jin et al. 2012; Castelló-Mor et al. 2016; Buisson et al. 2018).

Evidence of relativistic winds in NLS1 has indeed been found (see, e.g., Hagino et al. 2016; Kosec et al. 2018c) and in some cases the strength of the absorption lines correlates with the variability of the ionizing continuum as expected for radiatively-driven winds (see, e.g., Matzeu et al. 2017; Parker et al. 2017; Pinto et al. 2018). However, these “ultrafast outflows” are very similar to those found in several AGN accreting at about the Eddington limit or 1-2 orders of magnitude below (see, e.g., Pounds et al. 2003; Reeves et al. 2003; Tombesi et al. 2010), which could be driven by magnetic fields (Fukumura et al. 2017) rather than radiation pressure (King & Pounds 2015). It is not easy to find and compare unique observable predictions of the theoretical wind models with the observations of winds. The study of the wind thermal stability can be a step forward in this field and, therefore, it is proposed in this paper.

1.2 Ultraluminous X-ray sources

The detailed study of accretion physics at extreme rates has been boosted in the last decade by extraordinary discoveries in the class of objects known as Ultraluminous X-ray sources (ULXs), currently the best examples of compact objects surpassing the Eddington limit for long periods of time. ULXs are bright, point-like, off-nucleus, extragalactic sources with X-ray luminosities above 10^{39} erg/s, resulting from accretion onto a compact object (Kaaret et al. 2017). Recent studies have shown that some ULXs are powered by accretion onto neutron stars with strong magnetic fields (10^9 – 10^{13} G, e.g. Bachetti et al. 2014; Fürst et al. 2016; Israel et al. 2017a,b; Carpano et al. 2018), which confirmed earlier speculation that ULXs are in majority stellar-mass compact objects ($< 100 M_\odot$) at or in excess of the Eddington limit (King et al. 2001; Poutanen et al. 2007; Gladstone et al. 2009; Middleton et al. 2013; Liu et al. 2013; Motch et al. 2014). A few ULXs might still host intermediate mass black holes (10^3 – $10^5 M_\odot$) at more sedate Eddington ratios (see, e.g., Greene & Ho 2007; Farrell et al. 2009; Webb et al. 2012; Mezcuca et al. 2016).

Before the discovery of ultraluminous pulsars (PULX) it was already thought that most ULXs were super-Eddington due to the presence of a strong turnover below ~ 7 keV in most ULX spectra (see, e.g., Stobbart et al. 2006; Bachetti et al. 2013). In the softest states of ULXs (e.g. in NGC 55 ULX) the spectral curvature may start as low as 0.7 keV (see, e.g., Gladstone et al. 2009). It is difficult to explain the presence of this turnover in combination with the high 10^{39} – 10^{41} erg/s luminosities invoking sub-Eddington accretion

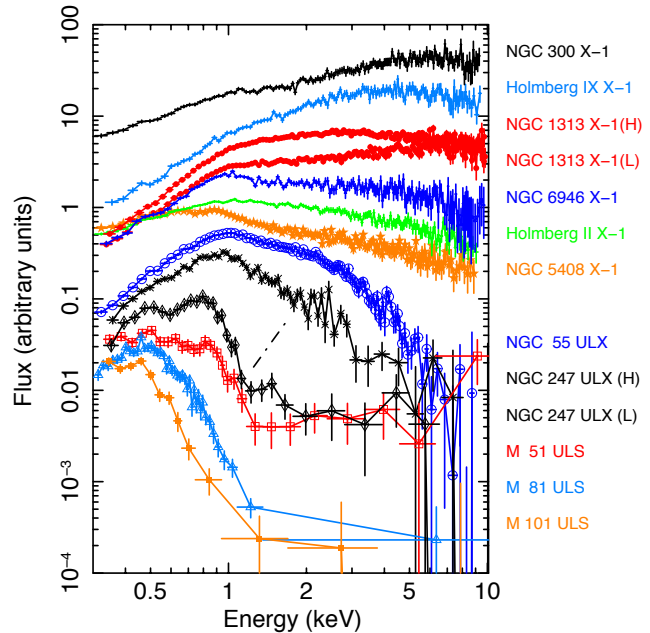


Figure 1. X-ray spectra of some among the brightest ULXs with hardness increasing from bottom to top. Y-axis units are $E \times F_E$, but the spectra were multiplied by constant factors - without altering the spectral shape - for displaying purposes. For NGC 1313 and 247 we show two remarkably different spectral states.

models. ULXs represent a very complex category of objects with spectra of different shapes and slopes. In Fig. 1 we show a hardness sequence of ULX X-ray spectra uncorrected for interstellar absorption similar to Pintore et al. (2017) and Pinto et al. (2017). When modelled with a power-law, the spectra show the photon index ranging from ~ 1 for the hardest ULXs, to 2.5 for the soft ULXs and above 4 for the ultraluminous supersoft sources (ULS or SSUL, see, e.g., Feng et al. 2016, Urquhart & Soria 2016).

In general, ULX broadband X-ray spectra require 2-3 emission components (with the hardest component possibly related to the accretion column onto the poles of a neutron star since it dominates when pulsations are detected; Walton et al. 2018). A broad blackbody-like emission with temperatures around 1 keV is likely produced by the supercritical thick disk itself, whose photon emission is highly distorted by hot electrons in the inner regions (up-scattering) and by down-scattering with cool electrons in the wind (see, e.g., Gladstone et al. 2009, Sutton et al. 2013 and Middleton et al. 2015a). A soft component with temperatures around 0.1 keV most likely arises from upper regions of the outer disk, where a radiatively-driven wind is expected to be launched at accretion rates comparable to or higher than the Eddington limit (see, e.g., Ohsuga et al. 2005; Poutanen et al. 2007; Takeuchi et al. 2013). It is also possible that some portions of the wind, particularly that one with much lower velocities, will be launched by thermal heating close to the Compton temperature (e.g., Begelman et al. 1983; Done et al. 2018).

1.2.1 The winds discovery and the unification scenario

The first discovery of powerful winds driven by radiation pressure in ULXs was achieved by the recent detection of

blueshifted absorption lines in high-resolution soft X-ray spectra provided by the *XMM-Newton* Reflection Grating Spectrometers (RGS, Pinto et al. 2016, 2017; Kosec et al. 2018a). Further confirmation was obtained in the Fe K hard X-ray energy band (Walton et al. 2016) and, in particular, for the ultraluminous X-ray pulsar NGC 300 X-1 (or NGC 300 PULX) both in the soft and the hard energy bands (Kosec et al. 2018b).

Several features were already seen, albeit spectrally unresolved, in the low-to-moderate resolution CCD spectra (see, e.g., Stobbart et al. 2006). The study of high-spatial-resolution *Chandra* data (Sutton et al. 2015) and timing variation (Middleton et al. 2015b) suggested that the residuals are mainly produced within a small region and are intrinsic to the ULX itself, providing the first evidence of a wind (see also Middleton et al. 2014).

On the basis of this theoretical, computational and observational evidence, a unification scenario has been proposed according to which ULX spectral properties depend on their accretion rates and inclination angles (see, e.g., Gladstone et al. 2009; Middleton et al. 2011, 2015a; Sutton et al. 2013) and on the ionization state and complexity of the wind in the line of sight (Pinto et al. 2017).

Fig. 2 shows an artistic impression of a wind blowing from the supercritical region of an accretion disk. In general, we should expect high ionization states of the wind at low inclinations from the disk rotation axis (on-axis) and progressively lower ionization at higher inclinations. However, the outflow is at least in part clumpy and optically thick, which implies that each line-of-sight (LOS) is dominated by a fraction of the wind exposed to a certain ionizing field and therefore characterized by a different thermal equilibrium.

So far, no work has focused onto the study of the thermal state of the winds in ULXs and its effect on the variability and detectability of the features imprinting the ULX X-ray spectra. This is crucial in order to probe and understand whether the proposed unification scenario actually works. This is further complicated as three-dimensional radiation-hydrodynamic simulations of outflows from supercritical accretion have shown that the wind is clumpy and may vary on very short (seconds) time scales (Kobayashi et al. 2018).

This paper is therefore dedicated to the study of the stability of ULX winds and their comparison to winds found in better known X-ray sources such as Narrow Line Seyfert 1, classical sub-Eddington Seyfert 1 nuclei and classical super-soft sources such as white dwarfs burning hydrogen (some of which are novae). This paper is structured as follows. We present the X-ray objects of this study in Sect. 2 and the computation of stability curves in Sect. 3. We discuss the results and provide insights on future X-ray missions in Sect. 4 and give our conclusions in Sect. 5. Some technical detail on our analysis is reported in Appendix A.

2 THE SOURCES

In this section we report the objects of our study. We include archetypal ULXs focusing on three cornerstone states (soft, intermediate, hard) represented by NGC 5408 X-1, NGC 1313 X-1 and the pulsar NGC 300 X-1. All three show evidence of outflows albeit at different statistical significance owing to the different exposure times (Pinto et al. 2016,

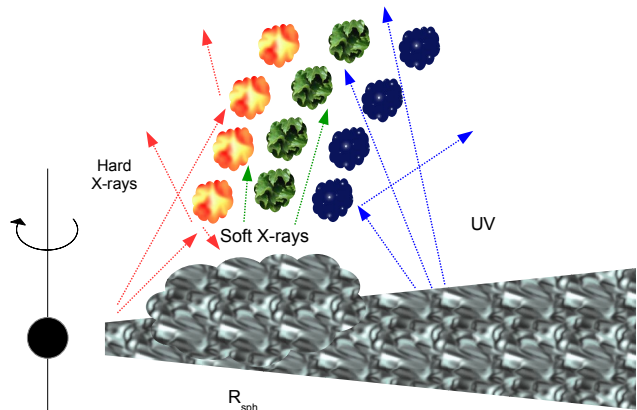


Figure 2. Schematic cartoon of a wind driven by radiation pressure in a super-Eddington accretion disk of a stellar mass black hole. The thickness of the disk and the high optical depth of the wind cause the inner portion of the wind to be exposed to a harder X-ray continuum compared to the outer regions, meaning that they are likely in a different thermal balance.

Kosec et al. 2018b). Some characteristics of these sources are shown in Table 1 along with other ULXs among the brightest ones and their highest significance wind components. These three sources have been observed with several satellites yielding broadband spectra covering the energy domain from IR to hard X-rays, which is necessary to compute photoionization balance. We also give examples of some other bright ULXs with similar spectral and timing behaviour.

On a broader context, we also want to compare ULX outflows to those found in other sources, particularly those where radiation pressure may play an important role (Table 2). Therefore, we include in our study the supersoft source nova V2491 Cygni, which exhibited a thick 3000 km/s outflowing envelope 40 days after its outburst (see, e.g., Ness et al. 2011 and Pinto et al. 2012) and the highly-accreting NLS1 IRAS13224-3809 that shows an ultrafast 0.2c outflow responding to continuum changes in agreement with theoretical models of radiation driven winds (Parker et al. 2017; Pinto et al. 2018).

We also test a blackbody spectrum with a temperature of 50 eV that mimics the observed spectra of super-soft ultraluminous X-ray sources (see, e.g., Urquhart & Soria 2016) and tidal disruption events (TDEs, e.g., Leloudas et al. 2016). A TDE is the disruption of a star that occurs near the event horizon of a ‘small’ supermassive black hole, $M_{\text{BH}} \sim 10^{5-7} M_{\odot}$. They are believed to reach fallback luminosities $100\times$ Eddington for a short period (e.g. Wu et al. 2018) and show evidence of radiation-pressure driven winds (see, e.g., Miller et al. 2015).

For useful diagnostics, we also incorporate the sub-Eddington Seyfert type 1 AGN NGC 5548 because the spectral code that we use (SPEX, Kaastra et al. 1996) has the photoionization balance calculation for this source as default (Steenbrugge et al. 2005) and was used in previous work on ULX winds (Pinto et al. 2016, 2017; Kosec et al. 2018a,b).

We will first compare the ULX NGC 1313 X-1 (where we found the first evidence of winds) to different types of non-ULX sources. Then we will focus on the thermal stability of ULX winds according to their ionization field.

Table 1. Characteristics of the brightest ULXs and *XMM-Newton* exposure times

Source	d (Mpc) ^(a)	L_X^{40}	Flux	HR	Wind	v_w	$\log \xi_w$	$t_{\text{exp}}^{\text{tot}}$ ^(b)	Similar sources
NGC 300 X-1	2.0	0.5	4	0.7	D	0.24	3.9	212	NGC 7793, NGC 5907, M 82 (PULXs)
Holmberg IX X-1	3.8	4	15	0.6	T	0.23	4.5	161	IC 342 X-1, NGC 1313 X-2
NGC 1313 X-1	4.2	2	5	0.5	D	0.19	2.3	750	NGC 5204 X-1
NGC 5204 X-1	4.8	1	2	0.4	D	0.34	3.0	160	NGC 1313 X-1
NGC 5408 X-1	5.3	1	3	0.2	D	0.20	2.1	655	NGC 6946 X-1, Holmberg II X-1
NGC 55 X-1	2.0	0.2	3	0.1	D	0.19	3.3	120	NGC 247 X-1, M81 ULS

^(a) Distances are from the Nasa Extragalactic Database. Unabsorbed X-ray (0.3 – 10 keV) luminosities L_X^{40} are in units of ($10^{40} \text{ erg s}^{-1}$), observed fluxes are in units of $10^{-12} \text{ erg s}^{-1} \text{ cm}^{-2}$ and hardness ratios ($HR = L_{2-10\text{keV}}/L_{0.3-10\text{keV}}$) are estimated adopting a multi-component emission model for the XMM/EPIC-pn spectra of the observations with evidence of winds (see Fig. 1). The wind velocities are in units of speed of light and the ionization parameters $\log \xi_w$ are in units of erg/s cm. For more detail on the wind properties, see Table A2. ^(b) XMM/RGS total exposure time in ks. Wind detections are labelled as *D* (or *T*) if their significance is above (or below) 3σ .

Table 2. List of non-ULX sources used for comparison.

Source	Source type	L_{Edd} peak ^(a)	M_\odot
NGC 5548	Seyfert 1 / AGN	0.05	4×10^7 ^(b)
IRAS 13224	NLS1 / AGN	5	1×10^6 ^(c)
V2491 Cygni	Nova / WD	1	1.3 ^(d)
Blackbody	50 eV model	–	–

^(a) X-ray luminosity in units of Eddington limit (with systematic uncertainties $\Delta L_{\text{Edd}} \sim 50\%$). ^(b) Pancoast et al. (2014), ^(c) Alston et al. (2018), Pinto et al. (2018), ^(d) Hachisu & Kato (2009).

Here we do not consider different cases of obscured / unobscured AGN as a detailed analysis was already performed by Mehdipour et al. (2016) including a description of the systematics introduced by using various photoionization codes. Testing different codes, they found variations of 10–30% in the value of the ionization parameter of the winds and the optical depth of the absorption lines, which are difficult to detect with the current X-ray telescopes.

3 THERMAL STABILITY

The SPEX code¹ is a powerful package to compute ionization balance of high-energy astrophysical plasmas. In particular, the newly implemented *pion* code is optimized to perform instantaneous calculation of ionization balance in the regime of photoionization, modelling simultaneously the input continuum and the emission/absorption lines produced by the ionized gas.

Photoionization equilibrium is parametrized with the well known relationship

$$\xi = \frac{L_{\text{ion}}}{n_H R^2} \quad (1)$$

where ξ is the ionization parameter (a measure of the number of photoionizing photons per particle), L_{ion} the ionizing source luminosity (usually taken between 1 and 1000 Rydberg, i.e. 13.6 eV and 13.6 keV), n_H the hydrogen density and R the distance between the plasma and the ionizing source (see, e.g., Krolik et al. 1981). A crucial input

to the photoionization calculation is therefore the ionizing continuum or the broadband spectral energy distribution (SED). The ionization balance also slightly depends on element abundances; here we adopt the recommended proto-Solar abundances of Lodders & Palme (2009), which are also the default in SPEX.

3.1 Spectral energy distribution

In order to build the SEDs of our sources we extract fluxes through all the available data from optical to hard X-ray energies. In Fig. 3 (top) we compare the SED of ULX NGC 1313 X-1 with the SEDs of the other non-ULXs sources detailed in Table 2. All SEDs have been corrected for interstellar absorption and E(B-V) reddening.

Briefly, we take the time-averaged XMM-Newton and NuSTAR X-ray spectra of IRAS13224-3809 from Parker et al. (2017) and the optical/UV data from the optical monitor (OM) time-average fluxes (Buisson et al. 2018). For NGC 5548 we use the default unobscured SED used by SPEX (Steenbrugge et al. 2005), while for nova V2491 Cygni we adopt the SED produced in Pinto et al. (2012).

For NGC 1313 X-1 we adopt the time-average XMM-Newton/EPIC spectrum (0.3–10 keV) where the wind was discovered (Pinto et al. 2016) along with the hard X-ray fluxes provided by NuSTAR (3–30 keV, Bachetti et al. 2013). Optical and UV fluxes are taken from Yang et al. (2011), whilst FUV fluxes are extracted from the XMM-Newton/OM using a 4 arc seconds circle onto its X-ray centroid and cross-checking with the source list produced by the XMM-SAS task OMCHAIN. The effects due to the time variability of the SED and the optical/UV fluxes of NGC 1313 X-1 are explored in Sect. 3.4–3.5.

For the other two ULXs, namely NGC 5408 X-1 and NGC 300 X-1 we use the X-ray spectra from Pinto et al. (2016) and Kosec et al. (2018b), respectively (see also Table A1). Optical and UV fluxes are obtained from HST measurements published in the literature (Grisé et al. 2012, Lau et al. 2016, Villar et al. 2016) and from the optical monitor on board XMM-Newton where some literature data points are missing. We prefer data from HST observations which are deeper and have higher spatial resolution than XMM-Newton/OM. Overall, the SEDs of the three ULXs look rather smooth and do not show sharp jumps of flux when

¹ <https://www.sron.nl/astrophysics-spx>

compared to the other sources with more accurate measurements outside the X-ray band like AGN and novae, see Fig. 3 and 4. They resemble the broadened disk spectra in Sutton et al. (2013), which suggests that the fluxes should be accurate with uncertainties less than an order of magnitude, small enough to avoid dramatic uncertainties in the ionization balance calculations.

The X-ray portions of the SEDs for the three ULXs under investigation (NGC 1313 X-1, NGC 5408 X-1 and NGC 300 X-1) are determined by fitting the time-averaged XMM-Newton/pn spectrum with a multi-component model consisting of blackbody, multicolour blackbody and power-law as discussed in Sect. 1 (see also Kosec et al. 2018b). The blackbody component ($T \sim 0.15 - 0.25$ keV) fits the disk upper photosphere, the multicolour blackbody ($T \sim 1 - 3$ keV) reproduces the overall disk emission and the power-law ($\Gamma \sim 1.5 - 2.5$) accounts for emission from the inner disk (and eventual contribution from the accretion column onto a neutron star, see e.g. Walton et al. 2018). Neutral absorption from the Galactic interstellar medium and circumstellar medium near the ULXs is reproduced by the *hot* model in SPEX adopting a low temperature $T = 0.5$ eV (see, e.g., Pinto et al. 2013 and references therein).

3.2 NGC 1313 ULX and non-ULX objects

We compute the photoionization balance running the SPEX *pion* code version 3.05.00 onto all SEDs. In Fig. 3 (middle panel) we show the detail of the photoionization balance computation (i.e. the temperature T – ionization parameter ξ curves). Some differences can be distinguished between these curves such as the variable slopes at intermediate values of the ionization parameter ($\log \xi \sim 2 - 3$). The detail of how heating and cooling rates are computed for ULX NGC 1313 X-1 and, in particular, their trends with the ionization parameter can be found in Appendix A2.

However, a more informative diagram is provided by the stability curves. Those can be produced by computing the ratio between the radiation pressure (F/c) and the thermal pressure ($n_H kT$), which is given by $\Xi = F/n_H c kT = 19222 \xi/T$, with $F = L_{\text{ion}}/4\pi r^2$ (Krolik et al. 1981). The stability (or S) curves computed for our sample of sources are shown in Fig. 3 (bottom panel). The S curves are powerful diagnosis tools because along them heating equals cooling and, therefore, the gas is in thermal balance.

On the left side of the S curve cooling dominates over heating, whilst on the right side, heating dominates over cooling. Most importantly, where the S curve has a positive gradient, the photoionized gas is thermally stable or, in other words, small perturbations upwards in temperature will be balanced by an increase in cooling. Similarly, small perturbations downwards will be balanced by increase in heating. Instead, in the points on the S curve with a negative gradient, the plasma is thermally unstable and therefore any perturbation upwards (downwards) will cause further increase (decrease) of temperature with a dramatic change, if not loss, of the equilibrium. In principle, any two components on the S -curve with the same Ξ value are expected to be in pressure equilibrium.

The stability curves computed for the different sources (Fig. 3) show notable differences, with the harder sources exhibiting several unstable branches. Here with hard sources

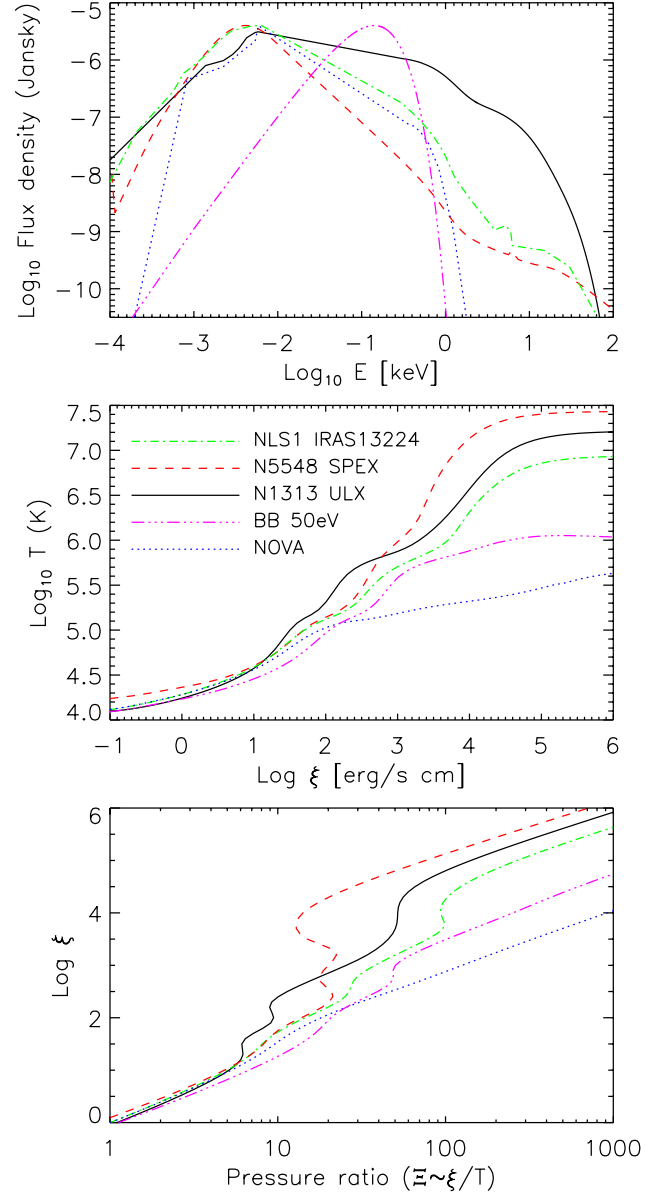


Figure 3. Spectral energy distribution (SED, top), T – ξ (middle) and stability curves (bottom) of ULX NGC 1313 X-1 compared to those of the AGN IRAS 13224 (NLS1) and NGC 5548 (SPEX), nova V2491 and a TDE-like 50 eV blackbody. The SEDs are normalized, multiplying for a constant, for displaying purposes.

we actually mean ‘X-ray hard sources’ i.e. those sources which have a high ratio between the fluxes calculated in the 2–10 keV and 0.3–2 keV energy bands, respectively. High-energy photons from the Fe K energy band and beyond significantly affect the ionization balance by increasing the size of the unstable region where, in principle, no plasma should be found (see also Krolik et al. 1981). On the other hand, the softest sources like novae or SSUL have rather stable curves. Moreover, the high-temperature turnovers differ by up to two orders of magnitude (Fig. 3, middle panel), which indicates great differences in the Compton temperature. Such variations are expected in objects of different accretion rates and are relevant for thermal and thermal-radiative winds

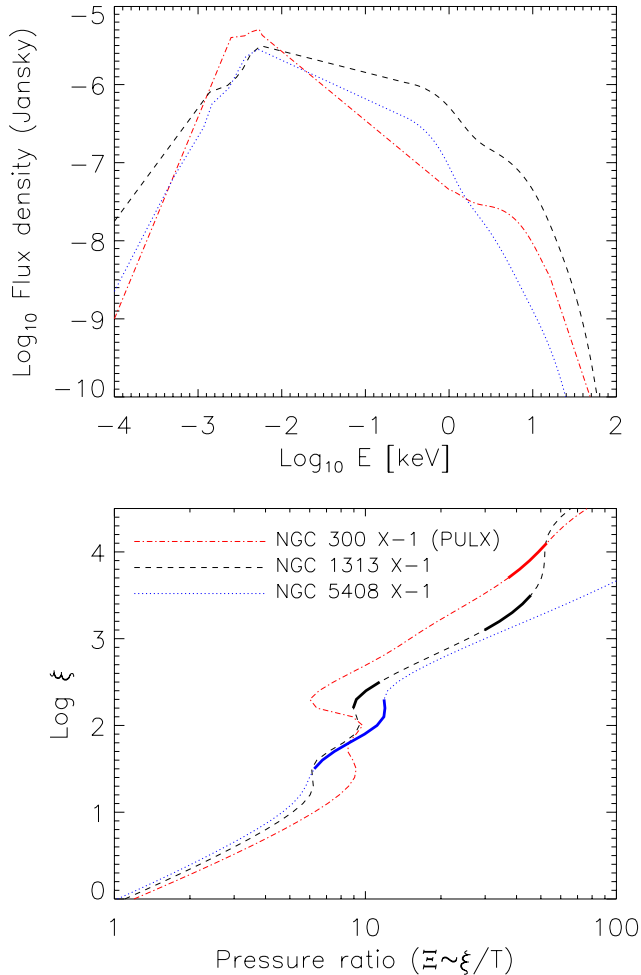


Figure 4. SEDs of three ULXs of different spectral hardness and the corresponding stability S curves. Thick regions on the S curves show the wind detections for these sources (Pinto et al. 2016; Walton et al. 2016; Kosec et al. 2018b). The SEDs have been normalized for displaying purposes similarly to Fig. 3.

since they can be suppressed if the Compton temperatures are too low (Done et al. 2018).

S curves of AGN (and classical X-ray binaries) have been studied in great detail and their instability branches are ubiquitously found (see, e.g., Krolik et al. 1981; Reynolds & Fabian 1995; Netzer et al. 2003; Steenbrugge et al. 2005; Chakravorty et al. 2016; Mehdipour et al. 2016; Higginbottom et al. 2017). Of course, owing to its SED, the stability curve of archetypal ULX NGC 1313 X-1 fits in between those of AGN and soft sources, showing only some small branches of instability.

3.3 NGC 1313 ULX and other ULXs

A comparison between the S curves of the intermediate-state ULX NGC 1313 X-1 with harder (Seyfert 1 AGN) and softer (supersoft source, SSS, nova) spectra provides a crude idea of how thermal instability increases for the wind parts which are subjected to harder SEDs. There is currently a strong likelihood that ULXs are characterized by geometrically-thick disks and optically-thick outflows, at least for ULXs

powered by black holes or neutron stars with limited magnetic fields (e.g. $< 10^{13}G$). It is therefore thought that the spectral hardness of a ULX is due to a combination of accretion rate and inclination. In fact, at lower inclinations (face on) we should see harder spectra (e.g., Middleton et al. 2015a; Feng et al. 2016; Urquhart & Soria 2016; Pinto et al. 2017).

It is very likely that the inner portions of the wind are exposed to a harder photoionizing field compared to the outer regions or, in other words, the inner regions may see beamed hard X-rays, while the radiation field in the outer regions may be dominated by UV and soft X-rays (see Fig. 2). If this scenario applies then the gas phases in these regions will have radically different stability curves.

In Fig. 4 (top) we compare the SEDs of three ULXs with different X-ray spectral shapes: NGC 300 PULX (hard), NGC 1313 X-1 (intermediate) and NGC 5408 X-1 (soft, see also Table 1). We have computed the ionization balance for the other two ULXs with the same code used for NGC 1313 X-1 in Sect. 3.2 and found significant differences in their stability curves (see Fig. 4, bottom). As expected, the harder ULX has longer branches of instability. This means that, according to the ULX unification scenario, there should be a systematic increase of instability for wind portions towards the inner regions of the accretion disk.

In Fig. 4 (bottom) we also indicate the ionization parameters and the corresponding pressure ratios of the winds detected in these ULXs on each S curve. For NGC 1313 X-1, there are two regions due to two alternative solutions for the Fe L and Fe K energy bands (Pinto et al. 2016; Walton et al. 2016, respectively). It appears that the wind ionization state increases with the spectral hardness of the source (and likely decreases with the viewing angle) and that the measurements are formally acceptable as none falls along instability branches. For NGC 5408 X-1, instead, the outflow has a more complex structure with two components of comparable ionization state ($\log \xi$ 1.5 – 1.9 and 1.7 – 2.1) but different velocities (Pinto et al. 2016; see also Table A2).

3.4 NGC 1313 ULX: Spectral Variability

We normally consider as classical ULXs those sources which surpass the Eddington limit of a 10 Solar mass black hole for long periods of time. However, these persistent beacons can show remarkable X-ray variability on time scales from hours to several days. PULXs for instance show long-term variability associated to either precession (see, e.g., Middleton et al. 2018) or switching between two different regimes that may be interpreted as a propeller phase (see, e.g., Tsygankov et al. 2016). Luminosities of ULXs can vary by an order of magnitude, followed by changes in the spectral slope by 20% or more (see, e.g., Kajava & Poutanen 2009). It is therefore a useful exercise to compute the ionization balance for ULXs where the spectral shape significantly changes with time in order to probe any effects on the wind stability (or on the portion of the wind in our line-of-sight).

Of course, NGC 1313 X-1 provides an excellent workbench thanks to the dozens of dedicated observations taken with XMM-Newton since early 2000s and owing to its high spectral variability (see, e.g., Middleton et al. 2015b). We therefore focus on three characteristic spectra of this ULX which show that the source alternates between soft-

ultraluminous, hard-ultraluminous and bright-broadened-disk states, respectively (according to the classification of Sutton et al. 2013; for more detail see Table A1).

NGC 1313 X-1 normally spends most of the time in the hard-ultraluminous state with intermediate brightness compared to the soft (X-ray faint) and the broadened-disk (X-ray bright) states. The corresponding SEDs are shown in Fig. 5 (top). For simplicity, we adopt the same values of optical and UV flux as given by the time-averaged SED (see Sect. 3.5 for a discussion on effects due to variable optical/UV fluxes). These broadband spectra represent a small sample, but they provide a good indication of how much the ionization field may vary and, therefore, how different will be the SED seen by the outflowing gas depending on its location (and our line of sight).

The standard continuum model consisting of absorbed powerlaw, blackbody and modified blackbody overestimates the flux below 1 keV due to the powerlaw steep index ($\Gamma \sim 2$). This effect is stronger for the X-ray bright and faint spectra (BBD and SUL, see Fig. 5 top) due to their strong spectral curvature and requirement of high column density (an order of magnitude above the interstellar value, $N_{\text{H,ISM}} \sim 5 \times 10^{20} \text{ cm}^{-2}$). For this reason, we cut their extrapolation below 1 keV forcing a flat plateau (see the blue dashed and red dashed-dotted lines). Alternatively, we also test another model where the powerlaw is substituted by another modified blackbody, i.e. $\text{hot} * (bb + mbb + mbb)$. This model reproduces the spectral curvature without the need of high neutral absorption (see the blue dashed-dotted and red dotted lines) and indicates the order of magnitude of uncertainty in the (unabsorbed) SEDs of these states. The intermediate, hard-ultraluminous state is not strongly affected by this issue and, therefore, we just keep the results obtained with the standard model.

We compute the ionization balance for these SEDs of NGC 1313 X-1 as done for the time-average spectrum and show the stability curves in Fig. 5 (bottom). As expected, the S curves significantly differ; in particular the broadened-disk SED exhibits a large instability branch for ionization parameters $\log \xi \sim 1.8 - 2.3$, which is smaller in the intermediate-hard state. The soft state shows instead a generally stable curve very similar to soft ULXs, novae and other SSS (see Fig. 3 and 4). The uncertainties in the SEDs due to the soft X-ray extrapolation do not seem to have drastic effects on the thermal stability of the wind.

3.5 NGC 1313 ULX and optical/UV screening

It is difficult to build a proper spectral energy distribution without simultaneous observations in all energy domains going from the optical to the X-rays. In most cases quasi-simultaneity with optical/UV data taken at slightly different time from the X-ray can provide reasonable measurements as we might expect the optical/UV not to vary on time scales as short as X-rays owing to the larger emitting region. In ULXs, of course, the scenario is complex as the bulk of the UV (and possibly the optical) emission may come from the outer disk itself but some contamination can be expected from the companion star (e.g., Grisé et al. 2012; Ambrosi & Zampieri 2018). Sutton et al. (2014) have shown that most objects at $\sim 10^{39} \text{ erg/s}$ exhibit disk reprocessing fractions similar to sub-Eddington objects, but at higher luminosities

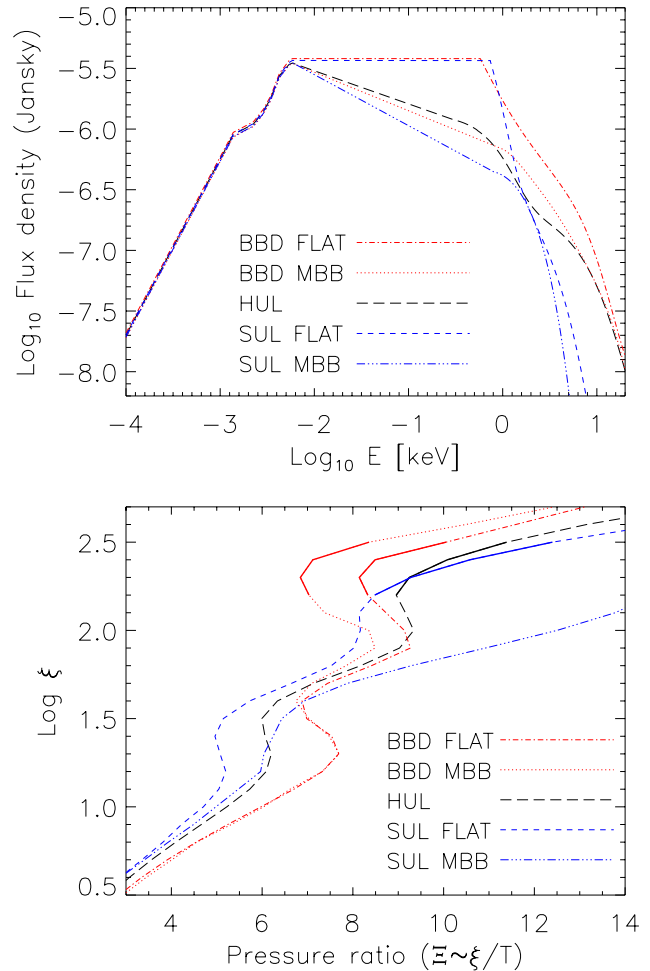


Figure 5. Spectral energy distribution (top) and stability curves (bottom) of ULX NGC 1313 X-1 calculated for different states (soft, SUL, bright-broadened-disk, BBD and hard ultraluminous, HUL; see Table A1). The solid intervals in the bottom plot indicate the RGS best fit wind solution (0.2c) obtained in Pinto et al. (2016). Two different continuum models for the BBD and SUL SEDs are tested here (see Sect. 3.4). During the brightest BBD state the gas might move towards an unstable branch.

ties X-ray reprocessing seems to increase, possibly due to scattering of wind X-rays back to the outer disk.

It is important to notice that the full optical-UV-X-ray SED that we observe might not actually be representative of the SED that ionizes all the different regions of the wind. The thick inner disk and even the wind itself may self-screen the inner regions of the wind from some of the optical/UV emission arising from the outer disk and the companion star.

Fig. 2 shows a simplified, qualitative, description of a radiation-driven wind from a super-Eddington accretion disk around a stellar-mass black hole or a neutron star. The temperature at the spherization radius can be roughly expressed as $T_{\text{sph}} = 1.5 m^{-1/4} \dot{m}_0^{-1/2} (1 + 0.3 \dot{m}_0^{-3/4}) \text{ keV}$ (see, e.g., Poutanen et al. 2007), which is of the order of 0.2 keV for a black hole with a mass $m = 10 M_{\odot}$ and an accretion rate $\dot{M} = 15 \dot{M}_{\text{Edd}}$. A comparable temperature is found in the soft X-ray component of almost all ULXs. Most X-rays

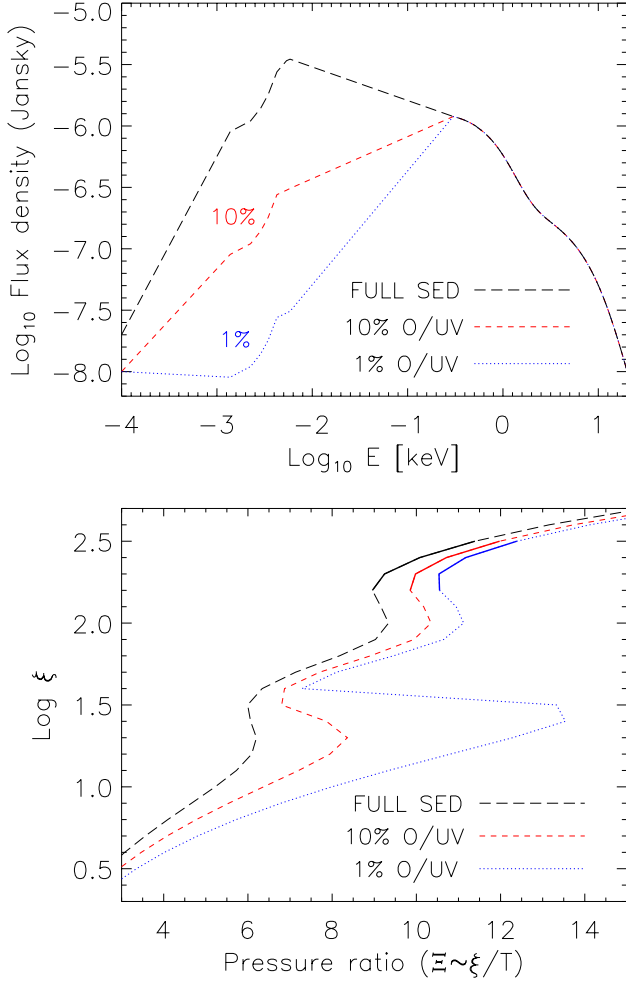


Figure 6. Spectral energy distribution (top) and stability curves (bottom) of ULX NGC 1313 X-1 calculated for the hard ultraluminous state, HUL (see Table A1), as compared to those in the cases where either 10% or 1% of the optical/UV flux reaches the absorbing gas. The solid intervals in the bottom plot indicate the RGS best fit wind solution (0.2c) obtained in Pinto et al. (2016). At high optical/UV screening, some portions of the wind could be unstable.

will be produced within T_{sph} , while at larger radii the flux will peak in the UV and optical energy bands.

The uncertainties in the SED shape and, particularly, in the UV/optical irradiation of the winds can be tested by computing the ionization balance for SEDs where the optical/UV fluxes are 1-2 orders of magnitude below the threshold measured with the XMM-Newton/OM or other facilities. We therefore construct ad-hoc SEDs with low-energy attenuation where only 1% or 10% of the optical/UV fluxes are transmitted and therefore received by the plasma in our LOS (see Fig. 6, top). This is a very simplified way to simulate partial covering of outer UV/optical photons by inner optically thick clouds. We use as template the SED of NGC 1313 X-1 during the most common hard-ultraluminous state where a wind was detected.

The stability curves show a progressive extension of the unstable branch for optical/UV transmission decreasing from 100% to 10% and then 1% (see Fig. 6, bottom). The

effects of optical/UV screening is however more pronounced at low ionization parameters ($\log \xi \lesssim 1.5$) which might not affect the current wind detection ($\log \xi \gtrsim 2.2$).

4 DISCUSSION

The most common AGN rarely reach the Eddington limit. Other extreme objects such as the tidal disruption events may reach fallback luminosities $100\times$ Eddington for a short period (e.g. Wu et al. 2018), but they are rare and difficult to observe due to their transient nature. It is also challenging to construct robust broadband SEDs for many AGN and TDEs because of extinction from neutral hydrogen, which mainly affects the energy range containing the SED peaks.

ULXs instead are X-ray bright and persistent, surpassing the Eddington limit for long periods of time. The search and study of radiatively driven winds in these sources may therefore provide clues on the way primordial black holes grew up when the Universe was a few hundred million years old. So far, no work has investigated the thermal stability of ULX winds and, therefore, in this paper we aim to understand their thermal state, their relationship with the LOS (that can change due to precession, e.g., Middleton et al. 2018) and the ULX state variability, which also depends on the accretion rate (e.g., Poutanen et al. 2007; Middleton et al. 2015a).

4.1 Thermal stability of winds in ULXs

In Sect. 3.1 we have shown broadband SED spectra of different types of sources (AGN, ULX, nova, etc). Then we have computed the ionization balance of plasma around ULXs for different spectral states and shown the stability curves, which indicate the combinations of $\xi - \Xi$ where the plasma is stable (Fig. 4). The winds detected in the three ULXs under investigation (i.e. NGC 300 PULX, NGC 1313 X-1 and NGC 5408 X-1) show $\xi - \Xi$ pairs corresponding to positive slopes of the S curve, which suggests that they are in stable equilibrium (as it would be required for them to be detectable).

It is important to notice that our results predict the existence of an evacuated funnel, which has been previously invoked in ULXs (e.g. Middleton et al. 2015a). In the innermost regions near the compact object, the wind likely becomes highly-ionized and/or thermally unstable, eventually disrupted, providing a better view on the hard X-ray emitting region.

4.2 ULX winds in a broader context

4.2.1 Comparison with winds from AGN and XRBs

There have been several studies dedicated to outflows in AGN and classical X-ray binaries, as well as their thermal stability in the past decades. Winds are better characterized in these objects owing to their high brightness due to either proximity (Galactic X-ray binaries) or huge luminosity (AGN). Below we report a brief summary on such winds.

AGN show a variety of winds detected in the UV such as the 0 – 5000 km/s warm absorbers (see, e.g., Reynolds & Fabian 1995; Steenbrugge et al. 2005; Laha et al. 2014),

the UV/X-ray obscurers that create temporary occultations and have comparable velocities (see, e.g., [Kaastra et al. 2014](#); [Mehdipour et al. 2017](#); [Turner et al. 2018](#)), the $\sim 10\,000$ km/s broad-absorption-line quasars (BALQSO, e.g., [Proga et al. 2000](#); [Hewett & Foltz 2003](#); [Dai et al. 2008](#); [Leighly et al. 2014](#)) and the most extreme $0.1\text{--}0.3c$ ultrafast outflows detected in the X-ray band (see, e.g., [Pounds et al. 2003](#); [Reeves et al. 2003](#); [Tombesi et al. 2010](#)). The highly ionized ultrafast outflows tend to occupy large branches of stability through the S curves (see, e.g., [Danehar et al. 2018](#); [Kraemer et al. 2018](#)), while the warm absorbers and the other winds with intermediate ionization states can fall near the regions of thermal instability ($\log \xi \sim 1\text{--}2$, see e.g. [Krolik et al. 1981](#); [Krongold et al. 2003](#); [Netzer et al. 2003](#); [Detmers et al. 2011](#)). The ultrafast outflows found in AGN are likely the most relevant comparison for the winds seen in ULXs as their similar properties (ξ , v_{outflow} , N_{H}) suggest some analogies in their launching mechanisms.

X-ray binaries often show highly ionized winds detected primarily in the Fe K band (see, e.g., [Miller et al. 2004, 2006](#); [Neilsen & Lee 2009](#); [Ponti et al. 2012](#)). These winds are slow (a few 100s km/s, therefore associated with the disk); they are often detected in the soft states and disappear when the source is in a hard state, most likely due to the instability branch that stretches further at harder ionizing SEDs (see, e.g., [Chakravorty et al. 2016](#); [Higginbottom et al. 2017](#)). However, an acceleration of the flow or the exhaustion of the plasma during the soft state are possible, viable solutions (see, e.g., [Gatuzz et al. 2019](#)).

SEDs of ULXs can significantly differ the one from the other, but they often show shapes resembling that of a broadened disk blackbody or of a complex, super-Eddington, accretion disk (see, e.g., [Gladstone et al. 2009](#); [Sutton et al. 2013](#); [Middleton et al. 2015a](#)). Their stability curves are halfway between those of high-Eddington NLS1 and super-soft novae, having only small branches of instabilities (see Fig. 3). The hard state ULXs such as the ultraluminous pulsar NGC 300 X-1 have in proportion a larger fraction of hard X-ray photons which further extend the unstable section (see Fig. 4). For PULXs with stronger magnetic fields, we can naturally expect more significant truncation of the inner accretion disk and strong polar inflow (at a given \dot{M}). This not only decreases radiation pressure in the inner regions of the disk, but can also produce a harder SED, followed by increasing instabilities in the inner portions of the wind. In other words, strongly-magnetized PULX will likely have weaker winds (i.e. with lower outflow rates) than weakly-magnetized PULXs for the same values of \dot{M} .

4.2.2 Effects of ULX winds on their surrounding

This study of ULX winds at small scales might be relevant to understand their effects at larger scales such as their role in the existence of ULX superbubbles with sizes of about ~ 100 pc that are thought to be similar to the (radio) W 50 nebula around SS 433 (e.g., [Pakull & Mirioni 2002](#); [Pakull et al. 2010](#)). For instance, [Pakull et al. \(2006\)](#) have shown that the bubbles have supersonic expansion speeds of 80–250 km/s, derived from the width of H α , which suggests that (at least some parts of) the bubbles are shock-excited by winds or jets rather than photoionized by X-rays from the central ULX (see also [Siwek et al. 2017](#)). They estimated that about

$10^{39\text{--}40}$ erg/s is required to ionize the optical bubbles. This is comparable to the estimates of wind kinetic power obtained in ULXs so far ([Pinto et al. 2016, 2017](#); [Walton et al. 2016](#); [Kosec et al. 2018a,b](#)):

$$\begin{aligned} L_w &= 0.5 \dot{M}_w v_w^2 \\ &= 2 \pi m_p \mu \Omega C \frac{v_w^3}{\xi} L_{\text{ion}} \sim 10^{39\text{--}41} \text{ erg/s} \end{aligned} \quad (2)$$

where $\dot{M}_w = 4 \pi R^2 \rho v_w^2 \Omega C$ is the outflow rate, Ω and C are the solid angle and the volume filling factor (or *clumpiness*), respectively, ρ is the density and R is the distance from the ionizing source. Here we have used Eq. (1) to get rid of the $R^2 \rho$ factor where $\rho = n_{\text{H}} m_p \mu$ with m_p the proton mass and $\mu = 0.6$ the average particle weight of a highly ionized plasma. A solid angle $\Omega/4\pi = 0.3$ and volume filling factor $C = 0.3$ were chosen as fiducial average values from MHD simulations of winds driven by radiation pressure in super-Eddington winds ([Takeuchi et al. 2013](#)).

Following the approach of [Pakull et al. \(2006\)](#), we know that the maximum mass ejected in the wind, $\dot{M}_w \tau$, throughout the ULX life time (τ) cannot be larger than the total mass transferred from the companion star to the Roche lobe of the compact object, which can be expressed as $m M_{\odot}$, where m is a factor of a few (for a standard high-mass companion star). From the wind kinetic luminosity L_w in Eq. (2) we can derive the wind velocity as

$$v_w = \sqrt{2 L_w / \dot{M}_w} \approx 0.19c \sqrt{L_{39} \tau_6 / m} \quad (3)$$

where L_{39} is the wind kinetic luminosity in units of 10^{39} erg/s and τ_6 is the ULX life time in 10^6 yr. This broadly agrees with the typical ULX wind velocities detected so far.

Alternatively, following the approach of [Castor et al. \(1975\)](#); [Weaver et al. \(1977\)](#); [Soker \(2004\)](#); [Begelman et al. \(2006\)](#), we can determine the expected radius of a bubble that has been inflated by a ULX wind. Assuming energy conservation, the bubble radius can be approximated as

$$R_{\text{bubble}} = 0.76 \left(\frac{\dot{M}_w v_w^2}{2 \rho_{\text{ISM}}} \right)^{1/5} \tau^{3/5} \quad (4)$$

where $\rho_{\text{ISM}} \sim 10^{-26}$ g cm $^{-3}$ is the interstellar density. If we adopt a wind kinetic power of a few 10^{39} erg/s, we obtain bubble with sizes of about 100 pc, which is consistent with the measurements quoted above.

These results have to be taken with some caution due to several uncertainties in the properties of both the winds and the bubbles. For instance, we adopt a lifetime of 10^6 yr from the size ~ 100 pc, the current expansion velocities of ~ 100 km/s and the expansion law $R \sim t^{3/5}$, but it is possible that in the past the bubbles were expanding faster. This would correspond to shorter lifetimes. We have adopted solid angles of 0.3, according to MHD simulations, but [Begelman et al. \(2006\)](#) suggest slightly lower values ($\Omega/4\pi = 0.1$). Finally, the total mass transferred from the companion to the compact object might be smaller than a solar mass ($m M_{\odot} < 1 M_{\odot}$). However, these uncertainties would tend to cancel each other out in the equations above. Our predictions of radii for the wind-inflated bubbles and of wind velocities are likely correct within the order of magnitude, which makes the comparisons meaningful. This would provide further evidence on the detection of winds in ULXs and their role on the surrounding environment.

Currently, the ULX wind sample is very small due to instrumental limitations and short exposure times. Once a larger sample would be available it will be of high interest to compare the presence of winds in ULXs with that of super-bubbles around them – and their characteristics – in order to better understand their formation.

4.3 Effects from inclination and accretion rate on the appearance of ULX winds

Fig. 2 shows an artistic impression of a wind launched from an accretion disk due to high radiation pressure. The wind gives the system a funnel geometry and scatters, i.e. geometrically beams, the X-ray photons coming from the inner regions (see, e.g., Poutanen et al. 2007; Middleton & King 2016). Therefore, we expect to see a hard X-ray spectrum followed by high ionization in the wind when the source is viewed at low inclinations (i.e. on-axis) and the more the inclination increases, the softer the X-ray spectrum and the lower the ionization of the wind should be, for a given accretion rate (e.g., Kawashima et al. 2012; Pinto et al. 2017).

We show the trend between the velocity and the ionization parameter of the winds with the spectral hardness in Fig. 7. We notice that a third of these detections were marginal ($\lesssim 3\sigma$, see those shown as diamonds) and that the results have to be taken with caution. We retrieve all the necessary information on the wind properties from previously reported detections and double-check the results with the newer SPEX version used in this paper. More detail on the wind data is reported in Sect. A3 and, particularly, in Table A2. We find a possible correlation between the ULX spectral hardness, HR , the wind ionization parameter, ξ , and velocity, v_w . We fit a straight line to the data using the PYTHON routine *odr*² that performs orthogonal distance regressions and obtained the following best fits:

$$\begin{aligned} v_w &= (0.06 \pm 0.04) + (0.46 \pm 0.15) HR \\ \log \xi &= (1.5 \pm 0.5) + (3.9 \pm 1.5) HR \end{aligned} \quad (5)$$

where HR is the hardness ratio. The Spearman and Pearson correlation coefficients range between 0.6 and 0.8 (see Table A3), which indicates a substantial positive correlation among the three parameters. Although there is significant scatter, the apparent trend is qualitatively consistent with the scenario for which we see hotter and faster wind component at lower inclination. The velocity trend may suggest that the optically-thin component of the wind (which is responsible for the blueshifted absorption lines) is likely not moving along the equatorial plane or, more simply, that at larger inclinations we see material expelled from an outer region where the escape velocity is naturally lower. The ULX wind sample is currently too small to obtain conclusive results, but our measurements agree with the general picture.

Some of the scatter is likely due to systematics. Here we show the (HR, ξ, v_w) values for the observations with statistics good enough to enable wind detections, but ULXs vary in hardness ratio. Therefore, we also show the HR fractional variability in Fig. 7 (blue large horizontal lines) as retrieved from the literature (see, e.g., Middleton et al. 2015a; Kosec

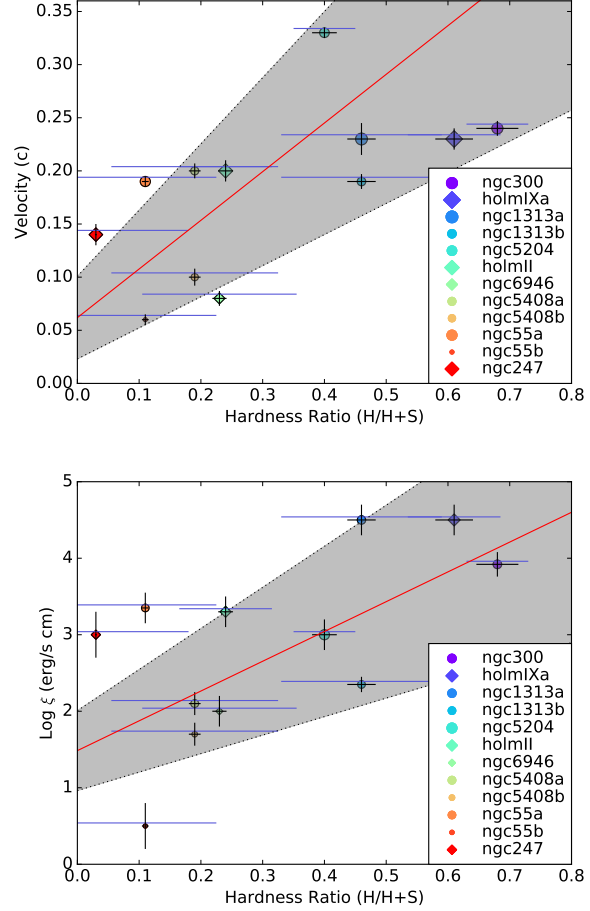


Figure 7. Trends of wind velocity (top) and wind ionization (bottom) versus spectral hardness in ULXs. Point-size and colour are coded according to the ionization parameter (top) and velocity of the wind (bottom). Circles and diamonds refer to significant ($> 3\sigma$) detections and tentative ($< 3\sigma$) detections, respectively. The shaded grey areas indicate the 1σ uncertainties of the best-fitting straight line (see the solid red lines). The larger blue horizontal bars show the spectral hardness variability of each ULX.

et al. 2018a,b; Pinto et al. 2017; Carpano et al. 2018 and references therein). Although, it might not be physically correct to fit a model to these points, the HR variability could still explain why they deviate from a tight correlation.

For the several reasons discussed above, the hard NGC 300 X-1, the intermediate NGC 1313 X-1 and the soft NGC 5408 X-1 ULXs are potentially being seen from increasing viewing angles. The comparison of their thermal stability curves in Fig. 4 would then confirm that the inner portions of the wind have to be necessarily more ionized and located along the $\xi - \Xi$ Compton cooling arm or they would disappear due to strong instabilities as often observed in the hard states of Galactic X-ray binaries (Chakravorty et al. 2016).

Super-orbital periods have been reported in several ULXs (see, e.g., Kaaret et al. 2006; Motch et al. 2014; Walton et al. 2016). These may be evidence of precession which suggests that different portions of the accretion disk and the wind would be visible to us at different times (see, e.g., Luangtip et al. 2016; Middleton et al. 2018). Variability

² <https://docs.scipy.org/doc/scipy/reference/odr.html>

in the accretion rate can cause similar behaviour because the scale-height of the flow, and thus the opening angle of the inner funnel, is expected to be related to the accretion rate (Poutanen et al. 2007). ULXs that have hard spectra at moderately-high accretion rates (dashed line in Fig. 5, top) could potentially undergo substantial obscuration of the inner region and appear softer after a large increase of accretion rate (dotted line). In principle, this should also strengthen the soft emission due to the outer disk emission (dotted line). At even higher rates or inclinations the ULX would look like a supersoft source (solid line).

In summary, either precession or variable accretion could expose our LOS to a wind portion whose ionizing field may be dominated by a region of the accretion disk with different average temperature. In Sect. 3.4, we have used the spectral variations of NGC 1313 X-1 to understand the effects of dramatic changes in the SED. When the source brightens from an intermediate-hard (HUL) state to the bright-broadened-disk state (BBD) and reaches its X-ray luminosity peak, the S curve changes, extending the region of instability and, therefore, affects the wind “warm” component with low ionization parameter ($\log \xi \sim 1.8 - 2.3$, dotted line in Fig. 5, bottom). This means that this wind component is either not in equilibrium or simply out of our LOS, in each case basically undetectable. This can explain the disappearance of the 1 keV residuals previously seen in Middleton et al. (2015b) and seems to be confirmed by new, deeper, XMM-Newton observations of NGC 1313 X-1 (Pinto et al. in prep).

It is worth to notice that the black holes powering AGN - which accrete at much lower Eddington rates than those in ULXs - exhibit ultrafast outflows within a broad range of inclination angles and their wind parameters do not show strong correlations with disk characteristics such as the inclination (see, e.g., Tombesi et al. 2014). This would suggest that AGN winds might differ from those seen in highly super-Eddington sources like ULXs, possibly due to a different launching mechanism. In fact, low-Eddington AGN winds are likely driven by magnetic pressure (see, e.g., Fukumura et al. 2017 and references therein).

We note that in this paper we have ignored effects due to ram pressure which can be relevant owing to the supersonic velocities of the winds. At high velocities ram pressure can equalise or even surpass thermal pressure if the outflow accelerates and/or changes direction due to magnetic fields. In the future we will investigate the effect of ram pressure by comparing our results with information on ram pressure from e.g. simulations of super-Eddington driven winds.

We also address briefly the possibility that some portions of the wind can be launched by thermal heating close to the Compton temperature (see, e.g., Begelman et al. 1983; Done et al. 2018). In our case, the Compton radius will be $R_{IC} = GM\mu/(kT_{IC}) \sim 3 \times 10^5 R_S$ for a $10 M_\odot$ black hole and $T_{IC} \sim 10^7$ K (i.e. the temperature where the $T - \xi$ curve flattens for the ULX in Fig. 3, middle panel). This is much larger than the spherization radius $R_{sph} = 5/3 \dot{M}k/(8\pi c) \sim 50 R_S$ and the photospheric radius $R_{phot} = \dot{M}_w k/(4\pi v_w \cos \theta) \sim 500 R_S$, the latter indicating where the wind becomes optically thin. Here we adopt $\dot{M} = 10 \dot{M}_{Edd}$, $\dot{M}_w = \dot{M}$, $v_w = 0.2c$, $\theta = 45^\circ$ and $\dot{m} = 10$ (see, e.g., Poutanen et al. 2007; Fiacconi et al. 2017). The hard X-rays from the inner region will likely be screened

by the thick disk atmosphere or the wind itself, and it will be difficult for them to reach the putative Compton radius (just like qualitatively shown in Fig. 2). Therefore, we do not expect to see a classical Compton wind with slow velocities (~ 500 km/s) from the outer disk.

4.4 Future missions: XRISM and ATHENA

XMM-Newton and Chandra have provided strong insights in the knowledge of ULXs and accretion physics in general since their launches 18 years ago. However, newly planned missions will significantly improve our ability to detect winds in these objects. XRISM³, for instance, will enable for the first time observations of ULXs with a good collecting area and an outstanding spectral resolution of about 5 eV in the hard X-ray band ($\sim 2 - 10$ keV), a combination missing in current telescopes (Guainazzi & Tashiro 2018).

Here we perform a simulation of NGC 1313 X-1 as it may be observed by XRISM using its predecessor Hitomi/SXS 5 eV response matrix (see Fig. 8, bottom panel). We adopt the best fit model from Pinto et al. (2016) consisting of a spectral continuum (blackbody $T = 0.3$ keV and powerlaw $\Gamma = 1.9$ components), an isothermal rest-frame collisionally-ionized plasma with a temperature of 0.8 keV, an outflowing photoionized plasma (column density $N_H = 5 \times 10^{21} \text{ cm}^{-2}$, $\log \xi = 2.3$, $v_{LOS} = 0.2c$, $v_{turb} = 500 \text{ km s}^{-1}$), and Galactic absorption through the *hot* model in SPEX with $N_H = 2 \times 10^{21} \text{ cm}^{-2}$ (see, e.g., Pinto et al. 2013). The simulation performed with the XRISM/Resolve microcalorimeter will provide a clear view of the Fe L region around 1 keV and boost the detection of lines above 2 keV with the resolution necessary to break degeneracy such as between the ionization parameter and the outflow velocity. However, we will still need observations of 100 ks or above in order to get 5σ significance detections for the strongest lines. Below ~ 0.7 keV the XMM-Newton/RGS grating spectrometer will still be the most sensitive instrument.

X-ray astronomy will radically change in the 2030s after the launch of ATHENA (Nandra et al. 2013; Guainazzi & Tashiro 2018). The mission will have both a wide field imager (WFI) with collecting area an order of magnitude above any current X-ray mission over the 0.3–10 keV energy band and a field of view of $40' \times 40'$, along with the X-ray Integral Field Unit (X-IFU). The X-IFU will be the first X-ray microcalorimeter to provide both high spatial ($5''$) and spectral (2.5 eV) resolution with an effective area an order of magnitude higher than any current high-spectral resolution X-ray detector. This corresponds to an improvement of almost 2 orders of magnitude in the way we detect and resolve narrow features in the canonical 0.3–10 keV X-ray energy band.

We perform another simulation of NGC 1313 X-1 using the same baseline model but only assuming an exposure time of 10 ks and the response matrix of ATHENA/X-IFU. The expected results are extremely promising (Fig. 8, top). Even a short exposure with X-IFU will provide a high signal-to-noise spectrum with a forest of emission and absorption lines all over the soft X-ray band, a spectrum quality comparable to the XMM-Newton/RGS spectra of very bright Galactic

³ X-Ray Imaging and Spectroscopy Mission, a.k.a. XRISM <https://heasarc.gsfc.nasa.gov/docs/xrism/>, to be launched in 2022

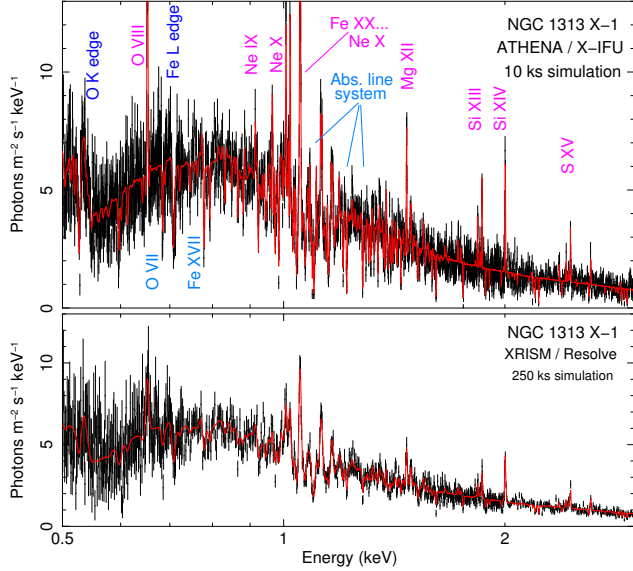


Figure 8. Simulations of the ULX NGC 1313 X-1 adopting the XMM-Newton/RGS best fit model from Pinto et al. (2016). Cosmic X-ray background and particle background are accounted for. The strongest transitions are labelled in the observed frame. We use the response matrix of *Hitomi*/SXS as a proxy for *XRISM*.

novae (see, e.g., Ness et al. 2011), with the remarkable difference that the ULX is located 4 Mpc away, while novae are within a few kpc from us.

The X-IFU spectrum will detect dozens of emission and absorption lines well above 5σ each and provide strong constraints on emission lines from triplets, such as Ne IX, and more lines sensitive to plasma density. More importantly, we will be able to detect winds in ULXs at much larger distance, therefore boosting the explored volume (dozens of ULXs with winds detections) and the wind parameter space including its energetics and variability. This will be crucial to fully address the relationships between the spectral hardness of the source and the wind properties already pointed in Eq. (5) and Fig. 7. It is also worth to mention that X-IFU will enable, for the first time, short-term variability studies of ULX winds and their connections with X-ray lags.

5 CONCLUSIONS

In this work we have provided the first insights on the thermal stability of winds in ultraluminous X-ray sources (ULXs), currently the best candidates of astronomical persistent sources to accrete beyond the Eddington limit. Using three archetypal ULXs with wind detections, we have probed the thermal stability for three strategic spectral states that broadly describe the ULX phenomenology: soft, hard and broadened-disk state. We have found that winds in ULXs are likely in stable thermal equilibrium with the harder states progressively extending the unstable branch. The stability curves resemble those of Narrow Line Seyfert 1 and super-soft sources as expected at high-Eddington rates. Our results predict the existence of the evacuated funnel in ULXs as the wind is unstable and/or highly-ionized in innermost regions, providing a better view of the hard X-ray region.

We have also investigated the consequence of X-ray spectral variability and, in general, dramatic variations in the ionizing field by studying some ad-hoc spectral states of ULX NGC 1313 X-1. The results have confirmed that over the periods of time where strong variability occurs (typically weeks-to-months in ULXs) the thermal stability also significantly varies, which can explain the disappearance of strong residuals (and therefore winds) during bright states. Precession and accretion rate changes could both contribute to this. We also find a possible correlation between the spectral hardness of the ULX, the wind velocity and the ionization parameter in support of the overall scenario and the geometry of super-Eddington accretion disks.

APPENDIX A: TECHNICAL DETAIL

Here we show some technical information that we avoid in the main body of the paper to facilitate the reading.

A1 Observation log

In Table A1, we report the XMM-Newton archival observations used to build the SEDs. In particular, the three longest observations taken during the intermediate-hard state where NGC 1313 X-1 spends most time and two specific observations yielding the softest and brightest state recorded for this source. The latter two have been used in Sect. 3.4 to compute the ionization balance of NGC 1313 for different spectral shapes (see Fig. 5). It is remarkable how NGC 1313 X-1 reaches extremely faint, soft states (e.g. for observation 0205230401) where its hardness ratio agrees (within error bars) with the brightest state of the supersoft ULX NGC 247 (see Table 1). This is of course expected from the unification scenario owing to a combination of lower accretion rates and system precession (see Middleton et al. 2015a for more detail on spectral variability of ULXs).

A2 Heating and cooling rates

In Fig. A1 we show the heating and cooling rates computed for the broadband SED of NGC 1313 X-1 using the intermediate-hard time-average spectrum (see Sect. 3.1, Fig. 3 and Table A1). These rates are computed using the *SPEX pion* code. These plots help to understand the behaviour of different physical processes at different ionization parameters, i.e. in different wind conditions. For our calculations, we set the hydrogen density to $n_H = 10^8 \text{ cm}^{-3}$ and the total column density to $N_H = 10^{22} \text{ cm}^{-2}$ similarly to Mehdipour et al. (2016). We notice that in the regime of non-optically-thick gas the main effect of the density is a systematic scaling of all heating and cooling rates.

At first, we notice that the total heating and cooling rates are broadly consistent, which means that a converging, equilibrium solution is found at nearly any value of the ionization parameter, ξ . At low ξ the dominant processes are heating by photo-electrons and cooling by collisional excitation. At high ξ the largest contribution to heating is given by Compton scattering and to cooling by inverse Compton scattering. There is therefore a radical change in

the dominant physical process with the ionization parameter and, therefore, the wind temperature. This is consistent with what [Mehdipour et al. \(2016\)](#) found comparing blackbody-like SEDs to harder spectra of AGN where other processes, such as Auger electrons and recombination, provide more significant contribution to heating and cooling, respectively. They also compared the results obtained by *SPEX pion* with those using different spectral codes such as *XSTAR* and *CLOUDY*, finding some interesting differences of 10–30% in the corresponding estimates of ξ and the concentration of several ionic species. However, they argue that these differences are unlikely to impact the scientific interpretation of current (AGN) outflow observations.

A3 Wind properties in ULXs

In Table A2 we quote the hardness ratios of each source calculated as $HR = L_{2-10\text{keV}}/L_{0.3-10\text{keV}}$ using a *bb+mbb+pow* spectral continuum (soft blackbody + broad modified blackbody + powerlaw, see e.g. [Kosec et al. 2018b](#)) for the XMM/EPIC-pn spectra from observations with evidence of winds (see Fig. 1 and Sect. 1.2). We also report the velocities and the ionization parameters of the wind along with the references used. These data are used to produce Fig. 7.

For NGC 5204 X-1 we fit the data with the new *pion* model in emission adopting $\Omega = 2\pi$ in order to obtain a measurement of the ionization parameter (see, e.g., [Psaradaki et al. 2018](#)). This is done because [Kosec et al. \(2018a\)](#) show spectral fits using only line-emission from gas in collisional equilibrium, which reproduces the lines better than photoionization equilibrium (but deeper observations are necessary to distinguish between a collisionally-ionized and a photo-ionized nature of the outflow).

For NGC 1313 X-1 we use the fastest and the slowest solutions found by [Pinto et al. \(2016\)](#) and [Walton et al. \(2016\)](#) because they yield the best description of the soft and hard X-ray components of the wind and also provide an idea of the systematic uncertainties.

We double-check the values for Holmberg II X-1, Holmberg IX X-1 and NGC 6946 X-1 by fitting the RGS+EPIC/pn spectra used in [Kosec et al. \(2018a\)](#) and [Pinto et al. \(2016\)](#). Here, we report the results obtained for the solution that correspond to the highest significance. We still quote the wind detection in these sources as tentative because the Monte Carlo simulations yield a significance below 3σ , likely owing to the limited statistics. The previous results have all been double-checked by testing the new version of *SPEX* used in this paper (3.05.00).

In Table A3 we quote the Spearman and Pearson correlation coefficients for the relationships between the ULX spectral hardness, HR , the wind ionization parameter, ξ , and velocity, v_w . They are calculated using the *scipy.stats.spearmanr* and *scipy.stats.pearsonr* PYTHON routines for the dataset shown in Table A2. Despite the large scatter, the results indicate a substantial positive correlation among the three parameters, which agrees with the predictions for super-Eddington disk geometry and winds.

Table A1. XMM-Newton observations used to build ULX SEDs.

Source	State	HR	OBS.ID	$t_{\text{exp}}^{\text{tot}}$ (ks)
NGC 300	Hard	0.7	0791010101	201.0
NGC 300	Hard		0791010301	
NGC 1313	Int-Hard		0405090101	
NGC 1313	Int-Hard	0.5	0693850501	345.6
NGC 1313	Int-Hard		0693851201	
NGC 1313	Bright-BB		0301860101	
NGC 1313	Low-Soft	0.04	0205230401	14.3
NGC 5408	Soft		0302900101	
NGC 5408	Soft		0500750101	
NGC 5408	Soft	0.2	0653380201	644.9
NGC 5408	Soft		0653380301	
NGC 5408	Soft		0653380401	
NGC 5408	Soft		0653380501	

Notes: Exposure times refer to the RGS 1,2 average. Unabsorbed hardness ratios (HR) are computed as $L_{2-10\text{keV}} / L_{0.3-10\text{keV}}$. The broadband SEDs are shown in Fig. 4 and 5.

Table A2. Wind properties and spectral hardness in ULXs

Source	HR	v_w	$\log \xi_w$	REF
NGC 300 X-1	0.68 ± 0.03	0.24 ± 0.01	3.9 ± 0.2	[5]
Holmberg IX X-1	0.61 ± 0.03	0.23 ± 0.01	4.5 ± 0.2	[4]
NGC 1313 X-1 (a)	0.46 ± 0.02	0.23 ± 0.02	4.5 ± 0.2	[1,3]
NGC 1313 X-1 (b)	0.46 ± 0.02	0.19 ± 0.01	2.3 ± 0.1	[1,3]
NGC 5204 X-1	0.40 ± 0.02	0.34 ± 0.01	3.0 ± 0.2	[4]
Holmberg II X-1	0.24 ± 0.01	0.20 ± 0.01	3.3 ± 0.2	[4]
NGC 6946 X-1	0.23 ± 0.01	0.08 ± 0.01	2.0 ± 0.2	[1,4]
NGC 5408 X-1 (a)	0.19 ± 0.01	0.20 ± 0.01	2.1 ± 0.2	[1]
NGC 5408 X-1 (b)	0.19 ± 0.01	0.10 ± 0.01	1.7 ± 0.2	[1]
NGC 55 X-1 (a)	0.11 ± 0.01	0.19 ± 0.01	3.3 ± 0.2	[2]
NGC 55 X-1 (b)	0.11 ± 0.01	0.06 ± 0.01	0.5 ± 0.3	[2]
NGC 247 X-1	0.03 ± 0.01	0.14 ± 0.01	3.0 ± 0.3	[2]

Hardness ratios ($HR = L_{2-10\text{keV}}/L_{0.3-10\text{keV}}$) are estimated adopting a *bb + pow + mbb* spectral continuum model for the XMM/EPIC-pn spectra from the observations where winds were found (see Fig. 1 and Sect. 1.2). (a,b) refer to different wind components found in the same source. The wind line-of-sight velocities are in units of speed of light, c , and the ionization parameters $\log \xi_w$ are in units of erg/s cm . The references are [1] [Pinto et al. \(2016\)](#), [2] [Pinto et al. \(2017\)](#), [3] [Walton et al. \(2016\)](#), [4] [Kosec et al. \(2018a\)](#) and [5] [Kosec et al. \(2018b\)](#).

Table A3. Wind properties and spectral hardness correlations

Parameters	Spearman	Pearson
$HR - v_w$	0.71	0.61
$HR - \log \xi_w$	0.58	0.62
$v_w - \log \xi_w$	0.76	0.70

Spearman and Pearson correlation coefficients calculated for the trends between Hardness ratios HR , wind components velocity v_w and ionization parameter $\log \xi_w$. See also Table A2 and Fig. 7.

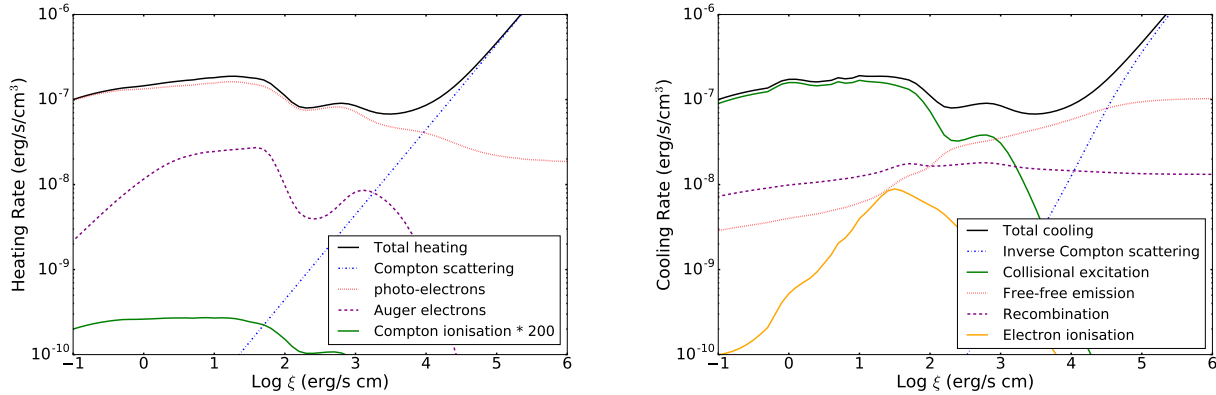


Figure A1. Heating rates (left panel) and cooling rates (right panel) calculated for NGC 1313 X-1 with the SPEX *pion* code.

ACKNOWLEDGMENTS

This work is based on observations obtained with XMM-Newton, an ESA science mission funded by ESA Member States and USA (NASA). CP is supported by European Space Agency (ESA) Research Fellowships. We acknowledge support from ERC Advanced Grant Feedback 340442, the European Union's Horizon 2020 Programme under the AHEAD AO5 project (grant agreement n. 654215) and the Faculty of the European Space Astronomy Centre (ESAC) under the project number 459. DJW and MJM thank STFC for support in the form of an Ernest Rutherford Fellowship. TPR acknowledges funding from the STFC via consolidated grant ST/P000541/1. We thank Jelle de Plaa for support in optimising SPEX, Douglas Buisson and William Alston for support with the XMM-Newton/OM. We also thank Manfred Pakull for useful discussions on the effects of ULX winds onto the surrounding bubbles and Ioanna Psaradaki for useful support with the PYTHON and the SPEX *pion* codes.

REFERENCES

- Aird J., Coil A. L., Georgakakis A., 2018, MNRAS, 474, 1225
- Alston W. N., Fabian A. C., Buisson D. J. K., Kara E., Parker M. L. e. a., 2018, MNRAS
- Ambrosi E., Zampieri L., 2018, MNRAS, 480, 4918
- Bachetti M., Harrison F. A., Walton D. J., Grefenstette B. W., Chakrabarty D. e. a., 2014, Nature, 514, 202
- Bachetti M., Rana V., Walton D. J., Barret D., Harrison F. A. e. a., 2013, ApJ, 778, 163
- Begelman M. C., King A. R., Pringle J. E., 2006, MNRAS, 370, 399
- Begelman M. C., McKee C. F., Shields G. A., 1983, ApJ, 271, 70
- Boroson T. A., 2002, ApJ, 565, 78
- Buisson D. J. K., Lohfink A. M., Alston W. N., Cackett E. M., Chiang C.-Y. e. a., 2018, MNRAS, 475, 2306
- Carpano S., Haberl F., Maitra C., Vasilopoulos G., 2018, MNRAS, 476, L45
- Castelló-Mor N., Netzer H., Kaspi S., 2016, MNRAS, 458, 1839
- Castor J., McCray R., Weaver R., 1975, ApJ, 200, L107
- Chakravorty S., Petrucci P.-O., Ferreira J., Henri G., Belmont R., Clavel M., Corbel S., Rodriguez J., Coriat M., Drappeau S., Malzac J., 2016, A&A, 589, A119
- Dai X., Shankar F., Sivakoff G. R., 2008, ApJ, 672, 108
- Danehar A., Nowak M. A., Lee J. C., Kriss G. A., Young A. J., Hardcastle M. J., Chakravorty S., Fang T., Neilsen J., Rahoui F., Smith R. K., 2018, ApJ, 853, 165
- Detmers R. G., Kaastra J. S., Steenbrugge K. C., Ebrero J., Kriss G. A., Arav N., Behar E., Costantini E., Branduardi-Raymont G., Mehdipour M., Bianchi S., Cappi M., Petrucci P., Ponti G., Pinto C., Ratti E. M., Holczer T., 2011, A&A, 534, A38
- Done C., Tomaru R., Takahashi T., 2018, MNRAS, 473, 838
- Fabian A. C., 2012, ARA&A, 50, 455
- Fan X., Strauss M. A., Schneider D. P., Becker R. H., White R. L. e. a., 2003, AJ, 125, 1649
- Farrell S. A., Webb N. A., Barret D., Godet O., Rodrigues J. M., 2009, Nature, 460, 73
- Feng H., Tao L., Kaaret P., Grisé F., 2016, ApJ, 831, 117
- Fiacconi D., Pinto C., Walton D. J., Fabian A. C., 2017, MNRAS, 469, L99
- Fukumura K., Kazanas D., Shrader C., Behar E., Tombesi F., Contopoulos I., 2017, Nature Astronomy, 1, 0062
- Fürst F., Walton D. J., Harrison F. A., Stern D., Barret D., Brightman M., Fabian A. C., Grefenstette B., Madsen K. K., Middleton M. J., Miller J. M., Pottschmidt K., Ptak A., Rana V., Webb N., 2016, ApJ, 831, L14
- Gatuzz E., Díaz Trigo M., Miller-Jones J. C. A., Migliari S., 2019, MNRAS, 482, 2597
- Gladstone J. C., Roberts T. P., Done C., 2009, MNRAS, 397, 1836
- Greene J. E., Ho L. C., 2007, ApJ, 656, 84
- Grimm H.-J., Gilfanov M., Sunyaev R., 2002, A&A, 391, 923
- Grisé F., Kaaret P., Corbel S., Feng H., Cseh D., Tao L., 2012, ApJ, 745, 123
- Guainazzi M., Tashiro M. S., 2018, ArXiv e-prints
- Hachisu I., Kato M., 2009, ApJ, 694, L103
- Hagino K., Odaka H., Done C., Tomaru R., Watanabe S., Takahashi T., 2016, MNRAS, 461, 3954
- Hewett P. C., Foltz C. B., 2003, AJ, 125, 1784
- Higginbottom N., Proga D., Knigge C., Long K. S., 2017,

- ApJ, 836, 42
- Israel G. L., Belfiore A., Stella L., Esposito P., Casella P. e. a., 2017a, *Science*, 355, 817
- Israel G. L., Papitto A., Esposito P., Stella L., Zampieri L. e. a., 2017b, *MNRAS*, 466, L48
- Jin C., Ward M., Done C., 2012, *MNRAS*, 425, 907
- Kaaret P., Feng H., Roberts T. P., 2017, *ARA&A*, 55, 303
- Kaaret P., Simet M. G., Lang C. C., 2006, *ApJ*, 646, 174
- Kaastra J. S., Kriss G. A., Cappi M., Mehdipour M., Petrucci P.-O., Steenbrugge K. C. e. a., 2014, *Science*, 345, 64
- Kaastra J. S., Mewe R., Nieuwenhuijzen H., 1996, in K. Yamashita & T. Watanabe ed., *UV and X-ray Spectroscopy of Astrophysical and Laboratory Plasmas SPEX: a new code for spectral analysis of X & UV spectra.* p. 411
- Kajava J. J. E., Poutanen J., 2009, *MNRAS*, 398, 1450
- Kawashima T., Ohsuga K., Mineshige S., Yoshida T., Heinzeller D., Matsumoto R., 2012, *ApJ*, 752, 18
- King A., Pounds K., 2015, *ARA&A*, 53, 115
- King A. R., Davies M. B., Ward M. J., Fabbiano G., Elvis M., 2001, *ApJ*, 552, L109
- Kobayashi H., Ohsuga K., Takahashi H. R., Kawashima T., Asahina Y., Takeuchi S., Mineshige S., 2018, *PASJ*, 70, 22
- Kosec P., Buisson D. J. K., Parker M. L., Pinto C., Fabian A. C., Walton D. J., 2018c, *MNRAS*, 481, 947
- Kosec P., Pinto C., Fabian A. C., Walton D. J., 2018a, *MNRAS*, 473, 5680
- Kosec P., Pinto C., Walton D. J., Fabian A. C., Bachetti M., Brightman M., Fürst F., Grefenstette B. W., 2018b, *MNRAS*, 479, 3978
- Kraemer S. B., Tombesi F., Bottorff M. C., 2018, *ApJ*, 852, 35
- Krolik J. H., McKee C. F., Tarter C. B., 1981, *ApJ*, 249, 422
- Krongold Y., Nicastro F., Brickhouse N. S., Elvis M., Liedahl D. A., Mathur S., 2003, *ApJ*, 597, 832
- Laha S., Guainazzi M., Dewangan G. C., Chakravorty S., Kembhavi A. K., 2014, *MNRAS*, 441, 2613
- Lau R. M., Kasliwal M. M., Bond H. E., Smith N., Fox O. D., Carlon R., Cody A. M., Contreras C., Dykhoff D., Gehrz R., Hsiao E., Jencson J., Khan R., Masci F., Monard L. A. G., Monson A. J., Morrell N., Phillips M., Ressler M. E., 2016, *ApJ*, 830, 142
- Leighly K. M., Terndrup D. M., Baron E., Lucy A. B., Dietrich M., Gallagher S. C., 2014, *ApJ*, 788, 123
- Leloudas G., Fraser M., Stone N. C., van Velzen S., Jonker P. G. e. a., 2016, *Nature Astronomy*, 1, 0002
- Liu J.-F., Bregman J. N., Bai Y., Justham S., Crowther P., 2013, *Nature*, 503, 500
- Lodders K., Palme H., 2009, *Meteoritics and Planetary Science Supplement*, 72, 5154
- Luangtip W., Roberts T. P., Done C., 2016, *MNRAS*, 460, 4417
- Matzeu G. A., Reeves J. N., Braitto V., Nardini E., McLaughlin D. E., Lobban A. P., Tombesi F., Costa M. T., 2017, *MNRAS*, 472, L15
- Mehdipour M., Kaastra J. S., Kallman T., 2016, *A&A*, 596, A65
- Mehdipour M., Kaastra J. S., Kriss G. A., Arav N., Behar E. e. a., 2017, *A&A*, 607, A28
- Mezcua M., Civano F., Fabbiano G., Miyaji T., Marchesi S., 2016, *ApJ*, 817, 20
- Middleton M. J., Fragile P. C., Bachetti M., Brightman M., Jiang Y.-F., Ho W. C. G., Roberts T. P., Ingram A. R., Dauser T., Pinto C., Walton D. J., Fuerst F., Fabian A. C., Gehrels N., 2018, *MNRAS*, 475, 154
- Middleton M. J., Heil L., Pintore F., Walton D. J., Roberts T. P., 2015, *MNRAS*, 447, 3243
- Middleton M. J., King A., 2016, *MNRAS*, 462, L71
- Middleton M. J., Miller-Jones J. C. A., Markoff S., Fender R., Henze M. e. a., 2013, *Nature*, 493, 187
- Middleton M. J., Roberts T. P., Done C., Jackson F. E., 2011, *MNRAS*, 411, 644
- Middleton M. J., Walton D. J., Fabian A., Roberts T. P., Heil L., Pinto C., Anderson G., Sutton A., 2015, *MNRAS*, 454, 3134
- Middleton M. J., Walton D. J., Roberts T. P., Heil L., 2014, *MNRAS*, 438, L51
- Miller J. M., Kaastra J. S., Miller M. C., Reynolds M. T., Brown G. e. a., 2015, *Nature*, 526, 542
- Miller J. M., Raymond J., Fabian A. C., Homan J., Nowak M. A., Wijnands R., van der Klis M., Belloni T., Tomsick J. A., Smith D. M., Charles P. A., Lewin W. H. G., 2004, *ApJ*, 601, 450
- Miller J. M., Raymond J., Homan J., Fabian A. C., Steeghs D., Wijnands R., Rupen M., Charles P., van der Klis M., Lewin W. H. G., 2006, *ApJ*, 646, 394
- Motch C., Pakull M. W., Soria R., Grisé F., Pietrzyński G., 2014, *Nature*, 514, 198
- Nandra K., Barret D., Barcons X., Fabian A., den Herder J.-W., Piro L., Watson M., Adami C., Aird J., Afonso J. M., et al. 2013, *ArXiv e-prints*
- Neilsen J., Lee J. C., 2009, *Nature*, 458, 481
- Ness J.-U., Osborne J. P., Dobrotka A., Page K. L., Drake J. J., Pinto C., Detmers R. G., Schwarz G., Bode M. F., Beardmore A. P., Starrfield S., Hernanz M., Sala G., Krautter J., Woodward C. E., 2011, *ApJ*, 733, 70
- Netzer H., Kaspi S., Behar E., Brandt W. N., Chelouche D., George I. M., Crenshaw D. M., Gabel J. R., Hamann F. W., Kraemer S. B., Kriss G. A., Nandra K., Peterson B. M., Shields J. C., Turner T. J., 2003, *ApJ*, 599, 933
- Ohsuga K., Mori M., Nakamoto T., Mineshige S., 2005, *ApJ*, 628, 368
- Pakull M. W., Grisé F., Motch C., 2006, in Meurs E. J. A., Fabbiano G., eds, *Populations of High Energy Sources in Galaxies Vol. 230 of IAU Symposium, Ultraluminous X-ray Sources: Bubbles and Optical Counterparts.* pp 293–297
- Pakull M. W., Mirioni L., 2002, *arXiv Astrophysics e-prints*
- Pakull M. W., Soria R., Motch C., 2010, *Nature*, 466, 209
- Pancoast A., Brewer B. J., Treu T., Park D., Barth A. J., Bentz M. C., Woo J.-H., 2014, *MNRAS*, 445, 3073
- Parker M. L., Pinto C., Fabian A. C., Lohfink A., Buisson D. J. K. e. a., 2017, *Nature*, 543, 83
- Pinto C., Alston W., Parker M. L., Fabian A. C., Gallo L. C., Buisson D. J. K., Walton D. J., Kara E., Jiang J., Lohfink A., Reynolds C. S., 2018, *MNRAS*, 476, 1021
- Pinto C., Alston W., Soria R., Middleton M. J., Walton D. J., Sutton A. D., Fabian A. C., Earnshaw H., Urquhart R., Kara E., Roberts T. P., 2017, *MNRAS*, 468, 2865
- Pinto C., Kaastra J. S., Costantini E., de Vries C., 2013, *A&A*, 551, A25
- Pinto C., Middleton M. J., Fabian A. C., 2016, *Nature*, 533, 64

- Pinto C., Ness J.-U., Verbunt F., Kaastra J. S., Costantini E., Detmers R. G., 2012, *A&A*, 543, A134
- Pintore F., Zampieri L., Stella L., Wolter A., Mereghetti S., Israel G. L., 2017, *ApJ*, 836, 113
- Ponti G., Fender R. P., Begelman M. C., Dunn R. J. H., Neilsen J., Coriat M., 2012, *MNRAS*, 422, L11
- Pounds K. A., Reeves J. N., King A. R., Page K. L., O'Brien P. T., Turner M. J. L., 2003, *MNRAS*, 345, 705
- Poutanen J., Lipunova G., Fabrika S., Butkevich A. G., Abolmasov P., 2007, *MNRAS*, 377, 1187
- Proga D., Stone J. M., Kallman T. R., 2000, *ApJ*, 543, 686
- Psaradaki I., Costantini E., Mehdipour M., Díaz Trigo M., 2018, *A&A*, 620, A129
- Reeves J. N., O'Brien P. T., Ward M. J., 2003, *ApJ*, 593, L65
- Reynolds C. S., Fabian A. C., 1995, *MNRAS*, 273, 1167
- Shakura N. I., Sunyaev R. A., 1973, *A&A*, 24, 337
- Siwek M., Sądowski A., Narayan R., Roberts T. P., Soria R., 2017, *MNRAS*, 470, 361
- Soker N., 2004, *A&A*, 414, 943
- Steenbrugge K. C., Kaastra J. S., Crenshaw D. M., Kraemer S. B., Arav N., George I. M., Liedahl D. A., van der Meer R. L. J., Paerels F. B. S., Turner T. J., Yaqoob T., 2005, *A&A*, 434, 569
- Stobbs A.-M., Roberts T. P., Wilms J., 2006, *MNRAS*, 368, 397
- Sutton A. D., Done C., Roberts T. P., 2014, *MNRAS*, 444, 2415
- Sutton A. D., Roberts T. P., Middleton M. J., 2013, *MNRAS*, 435, 1758
- Sutton A. D., Roberts T. P., Middleton M. J., 2015, *ApJ*, 814, 73
- Takeuchi S., Ohsuga K., Mineshige S., 2013, *PASJ*, 65, 88
- Tombesi F., Cappi M., Reeves J. N., Palumbo G. G. C., Yaqoob T., Braito V., Dadina M., 2010, *A&A*, 521, A57
- Tombesi F., Tazaki F., Mushotzky R. F., Ueda Y., Cappi M., Gofford J., Reeves J. N., Guainazzi M., 2014, *MNRAS*, 443, 2154
- Tsygankov S. S., Mushtukov A. A., Suleimanov V. F., Poutanen J., 2016, *MNRAS*, 457, 1101
- Turner T. J., Reeves J. N., Braito V., Lobban A., Kraemer S., Miller L., 2018, *MNRAS*, 481, 2470
- Urquhart R., Soria R., 2016, *MNRAS*, 456, 1859
- Vasudevan R. V., Fabian A. C., 2007, *MNRAS*, 381, 1235
- Villar V. A., Berger E., Chornock R., Margutti R., Laskar T., Brown P. J., Blanchard P. K., Czekala I., Lunnan R., Reynolds M. T., 2016, *ApJ*, 830, 11
- Volonteri M., Haardt F., Madau P., 2003, *ApJ*, 582, 559
- Walton D. J., Fürst F., Bachetti M., Barret D., Brightman M. e. a., 2016, *ApJ*, 827, L13
- Walton D. J., Fürst F., Heida M., Harrison F. A., Barret D., Stern D., Bachetti M., Brightman M., Fabian A. C., Middleton M. J., 2018, *ApJ*, 856, 128
- Walton D. J., Middleton M. J., Pinto C., Fabian A. C., Bachetti M. e. a., 2016, *ApJ*, 826, L26
- Weaver R., McCray R., Castor J., Shapiro P., Moore R., 1977, *ApJ*, 218, 377
- Webb N., Cseh D., Lenc E., Godet O., Barret D., Corbel S., Farrell S., Fender R., Gehrels N., Heywood I., 2012, *Science*, 337, 554
- Wu S., Coughlin E. R., Nixon C., 2018, *MNRAS*, 478, 3016
- Yang L., Feng H., Kaaret P., 2011, *ApJ*, 733, 118